

# Bayesian Optimization of Environmentally Sustainable Graphene Inks Produced by Wet Jet Milling

Lindsay E. Chaney, Anton van Beek, Julia R. Downing, Jinrui Zhang, Hengrui Zhang, Janan Hui, E. Alexander Sorensen, Maryam Khalaj, Jennifer B. Dunn, Wei Chen, and Mark C. Hersam\*

Liquid phase exfoliation (LPE) of graphene is a potentially scalable method to produce conductive graphene inks for printed electronic applications. Among LPE methods, wet jet milling (WJM) is an emerging approach that uses high-speed, turbulent flow to exfoliate graphene nanoplatelets from graphite in a continuous flow manner. Unlike prior WJM work based on toxic, high-boiling-point solvents such as n-methyl-2-pyrollidone (NMP), this study uses the environmentally friendly solvent ethanol and the polymer stabilizer ethyl cellulose (EC). Bayesian optimization and iterative batch sampling are employed to guide the exploration of the experimental phase space (namely, concentrations of graphite and EC in ethanol) in order to identify the Pareto frontier that simultaneously optimizes three performance criteria (graphene yield, conversion rate, and film conductivity). This data-driven strategy identifies vastly different optimal WJM conditions compared to literature precedent, including an optimal loading of 15 wt% graphite in ethanol compared to 1 wt% graphite in NMP. These WJM conditions provide superlative graphene production rates of 3.2 g hr<sup>-1</sup> with the resulting graphene nanoplatelets being suitable for screen-printed micro-supercapacitors. Finally, life cycle assessment reveals that ethanol-based WJM graphene exfoliation presents distinct environmental sustainability advantages for greenhouse gas emissions, fossil fuel consumption, and toxicity.

#### 1. Introduction

Emerging technologies such as wearable devices, point-of-care sensors, and the Internet of Things (IoT) promise to positively impact societal health, efficiency, and quality of life.[1-3] The continued proliferation and improvement of these miniaturized devices rely on innovative strategies for manufacturing flexible conductive electrodes and interconnects.[4] Additive manufacturing methods, such as gravure, screen, and inkjet printing, are promising fabrication routes for customizable electronic devices with micron-scale lateral resolution and square-meter-scale areal production capacity. These methods are also more costeffective with reduced waste compared to traditional subtractive manufacturing. [5,6] Among conductive printable inks, metal nanoparticles are the most widely employed functional materials. Although these inks can produce highly conductive features after sintering, they suffer from poor mechanical robustness and high cost,[7-9] which limit their widespread use in flexible, mass-produced microdevices. In

L. E. Chaney, J. R. Downing, J. Hui, E. A. Sorensen, M. Khalaj, W. Chen, M. C. Hersam

Department of Materials Science and Engineering Northwestern University

Evanston, IL 60208, USA

 $\hbox{E-mail: $m$-hersam@northwestern.edu}\\$ 

A. van Beek

School of Mechanical and Materials Engineering University College Dublin

Dublin D04 V1W8, Ireland



© 2024 The Authors. Small published by Wiley-VCH GmbH. This is an open access article under the terms of the Creative Commons Attribution-NonCommercial License, which permits use, distribution and reproduction in any medium, provided the original work is properly cited and is not used for commercial purposes.

DOI: 10.1002/smll.202309579

A. van Beek, H. Zhang, J. B. Dunn, W. Chen Department of Mechanical Engineering Northwestern University Evanston, IL 60208, USA

Evanston, IL 60208, USA J. Zhang, J. B. Dunn

Department of Chemical and Biological Engineering

Northwestern University Evanston, IL 60208, USA

J. Hui, M. C. Hersam Department of Chemistry Northwestern University Evanston, IL 60208, USA

M. C. Hersam

Department of Medicine
Department of Electrical and Computer Engineering

Northwestern University Evanston, IL 60208, USA



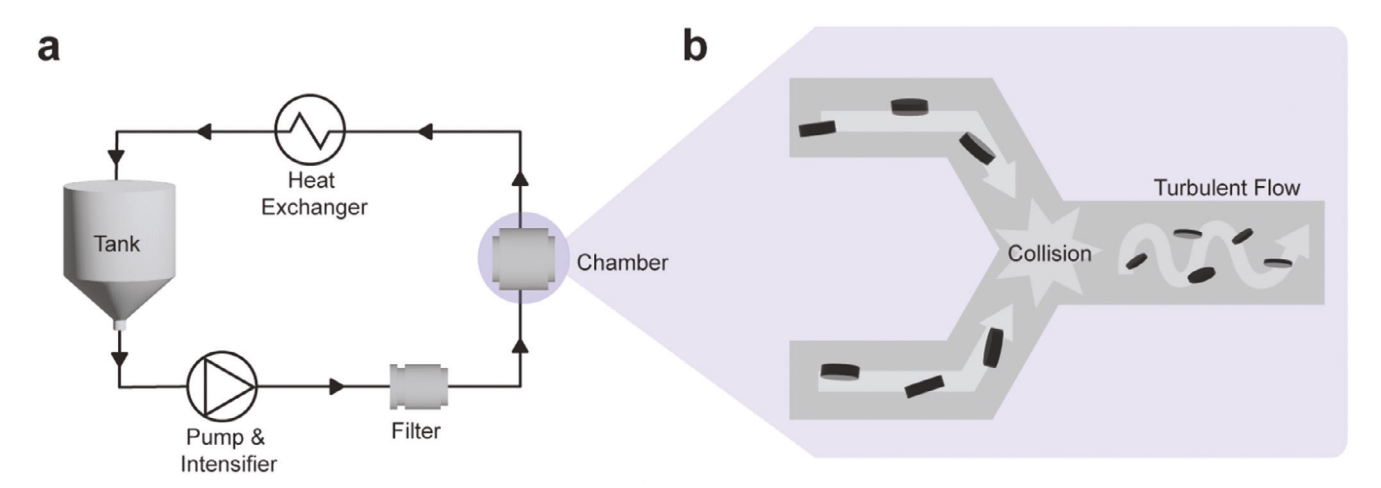


Figure 1. Overview of the wet jet milling system for graphene production. a) Process diagram depicting the continuous flow of graphite dispersion through the wet jet milling system during operation. b) Schematic of the graphite dispersion flow within the high-pressure collision chamber.

contrast, graphene inks have many advantages over incumbent metal nanoparticle inks, including improved mechanical flexibility, larger surface-area-to-volume ratio, lower cost, and higher chemical stability. These attributes make graphene a leading candidate for flexible, conductive electrodes in energy storage and sensing platforms.

However, graphene is challenging to produce in a scalable manner using common 2D material preparation techniques such as micromechanical cleavage and chemical vapor deposition.<sup>[13]</sup> Conversely, liquid phase exfoliation (LPE) can scalably exfoliate graphene from graphite via the application of shear forces in suitable solvents with production capacities spanning several volumetric orders of magnitude.<sup>[14]</sup> This scalability advantage has positioned LPE as the most industrially viable option for producing the sufficiently large quantities of graphene required by the large market for conductive inks. Moreover, LPE is easily integrated with downstream continuous-flow purification methods and subsequent patterning.<sup>[15,16]</sup>

Among LPE methods, wet jet milling (WJM) is one of the most recently introduced methods for graphene nanoplatelet production.[17,18] The technique has its origins in the food, cosmetic, and pharmaceutical industries for particle size reduction of powders.[19,20] Instead of relying on a grinding medium (e.g., blades, ball bearings) that may introduce contamination, WJM is unique in that it achieves size reduction via high-speed mutual collisions between solvent-suspended particles. During WJM, the raw dispersion enters a collision chamber where it is split into two streams that converge and collide at high pressure (Figure 1). Photographs and details of the WJM apparatus used in this study are provided in Figure S1 (Supporting Information). During graphene exfoliation, the impact of the mutual collisions fractures the graphite particles, and the subsequent high-speed, turbulent flow exfoliates layers from the graphite. As discussed in previous WJM reports, the exfoliation mechanism is similar to microfluidization, in which turbulent flow results in a dramatic velocity gradient orthogonal to the particle flow direction.[17,21] This gradient provides sufficient shearing forces to overcome the binding energy between adjacent graphite layers, resulting in exfoliated nanoplatelets. The WJM output stream is collected and subsequently centrifuged to remove unexfoliated material. The remaining graphene nanoplatelets are finally formulated into inks, which can be deposited via additive manufacturing methods to form percolating films. These mechanically flexible, highly conductive, and customizable graphene-printed films are typically combined with other electroactive components to form thin-film electronic devices.

The most notable previous demonstrations of WJM for graphene processing have employed the solvent n-methyl-2pyrrolidone (NMP).[17,18,22] The surface energy of NMP is wellmatched to bulk graphite powder, which promotes effective exfoliation and maintains a stable graphene colloidal dispersion. [23-25] However, NMP possesses several drawbacks including toxicity, negative environmental impacts, and a tendency to leave stubborn residues due to its high boiling point. In particular, sequestered NMP solvent in percolating networks of graphene flakes hinders electron pathways and lowers electrical performance.<sup>[26]</sup> While aqueous surfactant dispersions are a promising alternative, this approach often has inferior colloidal stability and also suffers from electrically insulating surfactant residues in percolating thin films. To overcome these limitations, polymers can be used as stabilizing additives to enable otherwise mismatched solvent-nanomaterial combinations.[27,28] Among the stabilizing polymer candidates, ethyl cellulose (EC) has emerged as the leading option for graphene dispersions based on environmentally benign alcohol solvents (e.g., ethanol).[29] Not only does EC promote exfoliation in ethanol to produce highstability graphene dispersions without toxic solvents, EC has also been shown to thermally or photonically decompose into an sp<sup>2</sup>rich char in the presence of graphene, which improves charge transport in percolating graphene films.[30,31]

Compared to other established methods such as sonication and shear mixing, WJM is a relative newcomer to the LPE land-scape. Therefore, an exploration of the broad parameter space for WJM is necessary to achieve optimal graphene exfoliation, especially for polymer-based dispersions that have not previously been pursued for WJM. Toward this end, here we report the optimization of WJM for EC-based graphene exfoliation in ethanol in an effort to achieve an environmentally friendly route to





www.small-journal.com

conductive graphene inks. Specifically, a Bayesian optimization (BO) model is employed to guide the efficient sampling of the WIM parameter space, resulting in notably high WIM graphene exfoliation yield and flake quality for printable graphene inks. While high-throughput combinatorial experiments that create large quantities of data are appropriate for certain optimization problems, [32] they are not practical when testing WJM due to the large quantities of raw materials and time-consuming characterization that are required. In contrast, active learning methods such as BO improve data efficiency by adaptively recommending sample areas of high interest. Furthermore, BO is tolerant to relatively high experimental uncertainty, which further reduces the experimental budget during process optimization. In particular, by explicitly considering both interpolation and experimental uncertainty using Gaussian process modeling, BO can correctly identify the optimal processing parameters with a limited number of experiments.

Unlike the work reported here, previous LPE optimization studies have employed a one-variable-at-a-time (OVAT) approach, which is both experimentally intensive and inefficient.[33-35] Additionally, when each variable is optimized in sequence, interdependence between variables is not considered and thus a global optimum cannot be guaranteed.[36] When considering multiple input parameters and responses, it becomes unfeasible to visualize the input-output relationships in a multivariable parameter space, thus precluding the ability to make optimal decisions on where to sample.[37] In contrast, efficient experimental design through BO can elucidate synergistic relationships between variables and address competing objectives in an unbiased manner. The relative importance of each objective may vary depending on the motives of individual stakeholders, but an impartial representation of the tradeoffs can streamline decision-making. For example, by extracting quantitative tradeoffs between yield, quality, cost, and environmental impact, the optimal compromise for all criteria can be reached more efficiently. Overall, a comprehensive exploration of the full design space of a promising LPE method like WJM is essential to realizing its potential as an industrial graphene production method. Considering the lack of a published methodology for WJM optimization, we aim to address this gap in the literature and provide guidance on efficient multi-objective optimization, which is crucial for the future of industrial-scale conductive graphene ink production.

After identifying the optimal WJM initial conditions, we then use screen printing for a demonstration of the resulting graphene inks because of its high throughput, compatibility with roll-to-roll processing, and industrial maturity.[38] Using our optimal exfoliation parameters, we produce high-quality screen-printing inks, which are then used to print interdigitated electrodes for planar micro-supercapacitor devices. These screen-printed microsupercapacitors exhibit excellent cycling behavior and achieve an areal capacitance of 513 µF cm<sup>-2</sup>, which is competitive with stateof-the-art graphene-based printed devices. Ultimately, by mapping LPE input parameters onto relevant property responses, we elucidate the processing-properties relationships in a multidimensional design space. With this BO-guided approach, we find that our optimal WJM graphite loading for EC-stabilized ethanol dispersions exceeds incumbent approaches based on NMP by 15-fold. With this expanded design space, we achieve a graphene production throughput of 3.2 g hr<sup>-1</sup> and establish WJM as a high-efficiency, continuous-flow LPE method. Overall, this work demonstrates that ethanol-based WJM graphene exfoliation presents distinct environmental sustainability advantages in greenhouse gas emissions, fossil fuel consumption, and toxicity for industrial-scale graphene production.

## 2. Bayesian Optimization

To efficiently determine the optimal WJM process control parameters, we employed a statistical framework to sequentially guide the search of the experimental phase space. In this section, we introduce the BO statistical models that provide an approximation of the target properties as a function of the WJM processing conditions. We then explain how these models can be leveraged to identify subsequent testing conditions in high-interest areas of the design space. We first introduce the general BO framework for an arbitrary multivariable optimization problem and then apply it specifically to ethanol-based WJM graphene exfoliation.

#### 2.1. General Approach

The adaptive sampling scheme as presented in Figure 2 consists of five steps. (Step 1) The process begins by initializing a design of experiments to generate a relatively small number of processing conditions that will be tested experimentally (e.g., factorial design, [39] optimal Latin hypercube sampling (OLHS), [40] or Sobol sequences<sup>[41]</sup>). In this work, we used OLHS to create an initial set of unique sampling locations of which some were replicated (i.e., repeated experiments with the same processing conditions). The advantage of repeated experiments is that they provide direct insight into experimental uncertainty. When only a subset of experiments is chosen to be replicated to conserve experimental resources, then their uniformity over the space of admissible processing conditions can be achieved by maximizing their minimum distance.<sup>[42]</sup> (Step 2) Once identified, this initial set of processing conditions is experimentally tested, and the measured properties are recorded. (Step 3) An approximation of the target properties as a function of the processing conditions is generated using a Gaussian process.<sup>[43]</sup> The advantage of using a Gaussian process is that it provides a predictive distribution of the target properties (i.e., mean and variance). In this work, we aim to find the spatial correlation between the processing conditions and the graphene properties, and the variance of the predictive distribution accounts for both the lack of data uncertainty and experimental uncertainty (more details are provided in the Supporting Information). (Step 4) The next batch of experiments is identified by maximizing an acquisition function.[44,45] The acquisition function leverages the predictive distribution of untested designs to systematically balance the need for exploration with exploitation. In other words, it balances the need to test unexplored regions in the space of admissible WJM processing conditions with the need to exploit nearby previously observed high-performing conditions. If a convergence criterion is not yet met, this new batch of experiments is tested, and the process is repeated (Steps 2-4). Examples of convergence criteria can include when the maximum acquisition function value is below a preset threshold or when a preset experimental budget has been exhausted.<sup>[46]</sup> In this work,



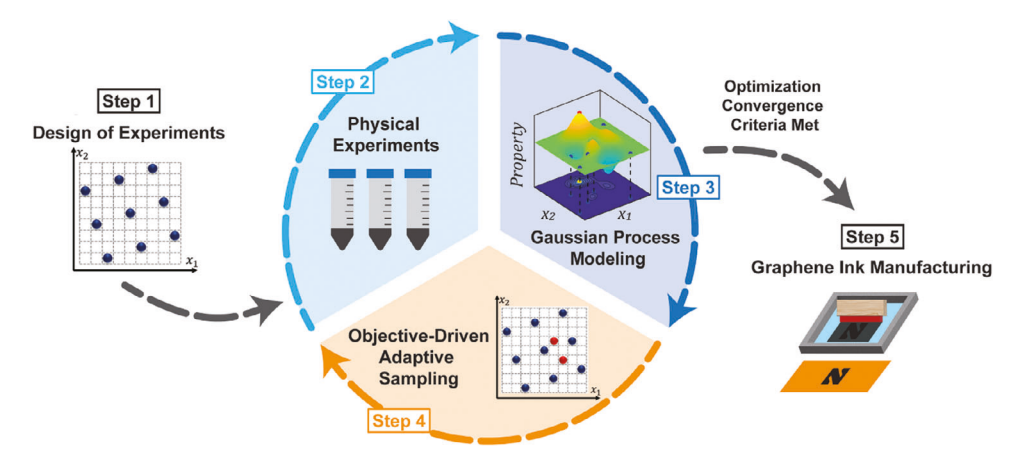


Figure 2. Bayesian optimization scheme. (Step 1) A design of experiments based on OLHS is initialized to generate a small number of processing conditions for testing. (Step 2) This initial batch of processing conditions is tested via physical experiments using WJM. (Step 3) An approximation of the target properties as a function of processing conditions is obtained using a Gaussian process. (Step 4) The next batch of experiments is identified by maximizing an acquisition function. If a convergence criterion is not yet met, this new batch of experiments is tested experimentally, and Steps 2–4 are repeated as necessary. (Step 5) Once the convergence criterion is met, the current approximation of the target properties is used to identify the optimal experimental conditions.

we establish an experimental budget of 14 initial samples (including five total replicate samples), and three subsequent batches of five samples each for a total of 29 samples. (Step 5) Once the convergence criterion is met, the current approximation of the target properties is used to define the optimal experimental conditions.

While adaptive sampling of computer experiments has been well studied, its extension to physical experiments as demonstrated here is still a challenging problem. The specific challenges considered in this paper include i) explicit consideration of the uncertainty in the collected data (i.e., experimental uncertainty);<sup>[47]</sup> ii) collection of batches of samples so that experiments can be performed in parallel;<sup>[48]</sup> and iii) design of testing conditions that considers multiple objectives associated with material properties (e.g., yield, conversion rate, and conductivity). In the remainder of this section, we introduce our method for approximating the target properties as a function of the WJM processing conditions in addition to explaining how this method is used to identify the next batch of testing conditions.

## 2.2. Target Property Approximation and Acquisition Function

The design of the WJM process conditions can be viewed as the following optimization problem:

$$\mathbf{x}^* = \underset{\mathbf{x} \in \mathcal{X}}{\operatorname{argmax}} f_{\mathbf{i}}(\mathbf{x}) \tag{1}$$

where  $\mathbf{x} = [x_1, \dots, x_p] \in \mathcal{X} \subset \mathbb{R}^p$  is a p dimensional vector of processing conditions that is defined on a space of admissible conditions  $\mathcal{X}$ ,  $f_i(\cdot)$  is the  $i^{\text{th}}$  (i=1,...,q) unknown target property, and  $\mathbf{x}^*$  are the optimal processing conditions. To solve this problem, we must approximate the unknown target property  $f_i(\cdot)$  through statistical inference. By conditioning a Gaussian process<sup>[43]</sup> on a set of observed responses  $\mathbf{Y}$  for processing conditions  $\mathbf{X}$ , we can approximate the target property  $f_i(\cdot)$  as  $Y_i(\cdot)|\mathbf{X},Y_i\approx \mathcal{N}(\hat{\mu}_i(\mathbf{x}),\hat{s}_i^2(\mathbf{x}))$ , where  $Y_i,\mu_i(\cdot)$  and  $s_i^2(\cdot)$  are the observed training responses, the mean approximation, and the vari-

ance of the *i*<sup>th</sup> response, respectively. While the predictive variance in Gaussian processes is known to account for the lack of data uncertainty, they can also account for the experimental uncertainty through an independent noise term that is added to the diagonal elements of the covariance matrix.<sup>[43]</sup> Assuming that the noise is constant over the space of admissible processing conditions (i.e., the experimental uncertainty is homoscedastic), only one additional parameter is introduced that needs to be inferred from the observed data. Consequently, under these assumptions, we are able to jointly account for the lack of data uncertainty and the experimental uncertainty when we only have access to a small number of experiments.

The process centers around leveraging the predictive mean and variance of the target properties to identify what additional experiments to perform with the purpose of reducing the number of costly experiments required to identify the globally optimal processing conditions. The next processing conditions are identified through the optimization of an acquisition function  $\alpha(x)$  using:

$$\mathbf{x}_{new} = \operatorname*{argmax}_{\mathbf{x} \in \mathcal{X}} \alpha \left( \mathbf{x} | \hat{\boldsymbol{\mu}}, \hat{\mathbf{s}}^2 \right)$$
 (2)

where  $\hat{\boldsymbol{\mu}} = \{\hat{\mu}_1, \dots, \hat{\mu}_q\}^T$  and  $\hat{s}^2 = \{\hat{s}_1^2, \dots, \hat{s}_q^2\}^T$ . For a single objective example, a new process condition to test is identified by maximizing  $\hat{\boldsymbol{\mu}}(\cdot)$  (i.e.,  $\alpha$  (·) =  $\hat{\boldsymbol{\mu}}$  (·)). However, this approach results in an algorithm that places too much trust in the fidelity of the initial target property approximation and runs the risk of getting stuck in a local optimum. Consequently, including the predictive variance ( $\hat{s}^2$ ) as a part of the acquisition function helps to remedy this issue by balancing the optimality of a potential processing condition with the magnitude of the predictive variance  $\hat{s}^2(\cdot)$ . While many examples of acquisition functions have been proposed in the literature (e.g., expected improvement, [49] knowledge gradient, [50] and predictive entropy search [51]), we use the modified expected improvement that is appropriate for noisy experimental data by considering the difference between

onditions) on Wiley Online Library for rules of use; OA articles are governed by the applicable Creative Commons

www.small-journal.com

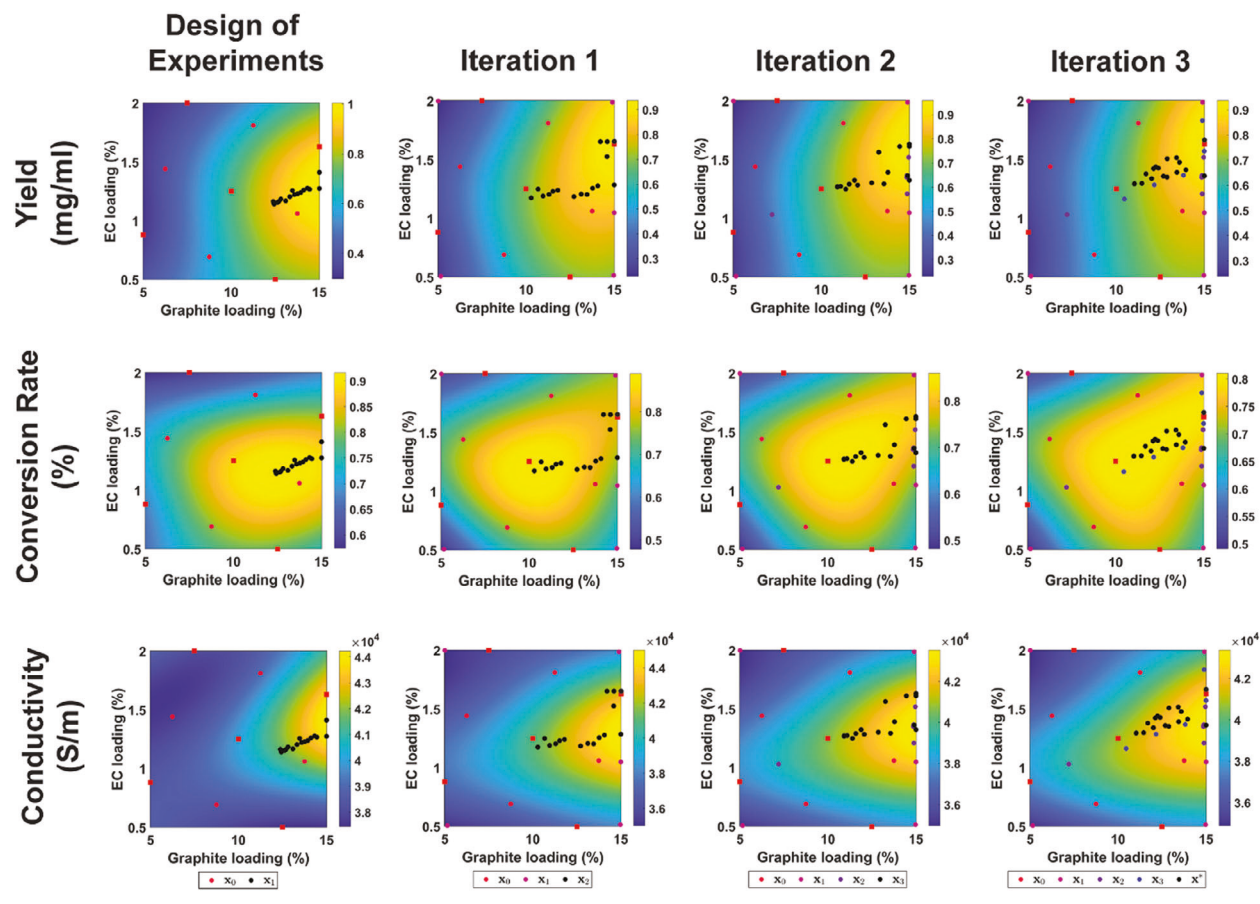


Figure 3. The mean approximations for graphene yield, graphene conversion rate, and graphene film conductivity generated by the Gaussian process model after each sampling iteration. The initial design of experiment cases (OLHS) are labeled red. Squares indicate experiments with duplicates. The experiments observed for later batches are colored according to the purple gradient. The black circles are the processing conditions associated with the Pareto frontier.

prediction uncertainty and data uncertainty. [52] Finally, to be compatible with multiple objectives (i.e., yield, conversion rate, and conductivity), we use the min-max improvement metric. This approach involves selecting the experimental condition that has the largest acquisition function value with respect to the input conditions (i.e., the maximum modified expected improvement) but has the smallest acquisition function value with respect to the current set of optimal target properties. Importantly, multiple target properties can be included concurrently as we are optimizing q=3 objectives (see Supporting Information for more details).

While the optimization problem in Equation (2) can be used to find the next processing condition to test, it is often desirable to identify a batch of experiments in an effort to save time, especially when experiments can be performed in parallel. To achieve this aim, we use a preposterior analysis that involves assuming that the predicted response at a newly identified design of processing conditions is correct. Subsequently, we can temporarily add this new observation  $[x_{\text{new}}, \hat{\mu}(x_{\text{new}})]$  to the training data set [X, Y]. This facilitates updating the approximation of the target properties to identify additional processing conditions without physically testing them. However, it should be noted that generating large batches of new experiments without testing runs the risk of wasting experimental resources. Consequently, we used a batch

size of five to gain a temporal advantage by performing experiments in parallel while limiting the negative consequence of the preposterior analysis.

# 3. Optimized Wet Jet Milling Conditions

The goal of this study is to achieve efficient, high-quality graphene production by establishing the relationship between relevant exfoliation variables and their property responses. While the framework presented in the previous section can be generalized to any multidimensional parameter space, we chose the following design because it is most relevant to the goals of electronic-grade graphene production. Specifically, the two input variables are 1) bulk graphite powder concentration and 2) EC stabilizer concentration, both in ethanol. Meanwhile, the three responses are 1) graphene yield, 2) graphene conversion rate, and 3) graphene film conductivity, all three of which are widely reported in LPE literature and are considered standard figures of merit (FOMs) for graphene production. [17,53,54] Importantly, these three competing responses cannot be simultaneously maximized without tradeoffs. Thus, it is valuable to identify the Pareto frontier, or the set of conditions for which no condition exists with improved properties for all three FOMs (i.e., the set of conditions





www.small-journal.com

**Table 1.** Optimal conditions were predicted for the three responses.

	Graphite loading [wt%]	EC loading [wt%]
Yield	15.0	1.7
Conversion rate	11.1	1.3
Conductivity	15.0	1.4
Weighted optimal	15.0	1.5

that are non-dominated). Specifically, yield (mg/mL) is a measure of total graphene mass produced per volume of solvent. This metric is most important when targeting solvent waste reduction and an increase in graphene production throughput. Conversion rate (%) is the ratio of graphite precursor converted to graphene during exfoliation, which is important when aiming to reduce graphite and EC precursor waste. Conversion rate also becomes crucial when it is unfeasible to begin with a high initial loading of raw materials in the solvent due to poor dispersion stability. Clearly, maximizing both yield and conversion rate concurrently is the ideal pathway toward achieving the largest quantities of graphene nanoplatelets (i.e., the highest graphene production throughput). However, these metrics cannot be fully maximized simultaneously without experiencing tradeoffs. Finally, film conductivity (S/m) is the experimentally measured conductivity of a percolating graphene film and is an indication of the graphene quality in printed electronics applications. While extracting flake population statistics from atomic force microscopy (AFM) images is another common metric for determining flake quality, the AFM workflow is time-consuming and impractical for the short timelines in optimization studies. Moreover, because our goal is to incorporate graphene nanoplatelets into inks for conductive electrodes, film conductivity is a more suitable quality metric during process optimization. AFM and other characterization techniques are only applied to the final optimized graphene nanoplatelet sample for confirmation purposes. Ultimately, the choice and relative importance of the FOMs for any system depends on the target application and manufacturing priorities.

#### 3.1. Bayesian Optimization Results

The mean target property approximations for each of the three outputs are plotted in Figure 3, and optimal input values are reported in Table 1. Based on the weighted average of all three property criteria, the optimal conditions were determined to be 15.0 wt% graphite and 1.5 wt% EC. As expected, it is clear that more EC must be supplied into the system to maintain colloidal stability, as evidenced by the universally low properties at low EC inputs. Another significant takeaway is that yield (the graphene produced per volume of solvent) is maximized at the maximum graphite loading, whereas graphene conversion rate (the fraction of graphite converted to graphene) is optimized at moderate graphite loadings. Because the graphite particles mutually collide to form freshly fractured surfaces that are more easily exfoliated, an increase in graphite loading results in more frequent collisions and thus higher conversion. However, a critical point exists at which excess graphite results in a decrease in conversion efficiency, which likely results from destabilization and reaggregation of the colloidal system as more flakes are exfoliated. Thus, while the concentration of graphene produced continues to increase at higher graphite loadings, the rate of conversion becomes less efficient with excess graphite.

Furthermore, while all experiments resulted in high film conductivity (>3.5  $\times$   $10^4$  S  $m^{-1}$ ), some significant trends were observed that further elucidate the processing-property relationships in the ethanol-EC system. Higher amounts of EC appear to be more difficult to thermally remove and lead to suboptimal film morphology, thus hindering electron transport. While it is well established that the thermal decomposition of EC results in a conductive carbon residue, these results indicate that excess EC is not a completely passive component in the system but can eventually compromise final electronic properties in the high concentration limit. Meanwhile, low initial EC loadings result in suboptimal ink characteristics and flake restacking, which decreases conductivity.

As discussed previously, the generated response surfaces in Figure 3 offer a holistic picture of the parameter space, including quantifiable tradeoffs between different processing conditions. While various stakeholders may judge the relative value of these metrics differently (e.g., prioritizing cost versus quality), the full picture can be used to make more informed decisions. This comprehensive view demonstrates the power of the generated target property approximations, as the model fully maps the entire multivariable design space with an input-output relation for all admissible processing conditions that can then be analyzed. [49]

Figure S2 (Supporting Information) plots the predicted Pareto frontier within the 3D output space for each iterative stage of the adaptive sampling process. In multi-objective optimization, the Pareto frontier represents the sets of conditions with nondominated objectives. The Pareto frontier markedly changes in the first two batches but settles into a stable location at the end of the study. This stabilization is further confirmed by quantifying the expected improvement after each new batch of data (Figure S3, Supporting Information), which plateaus in the later stages of the study. This plateauing indicates that the preset condition of four iterative sampling batches (i.e., 29 total samples) was sufficient to reach convergence. Other LPE studies using an OVAT framework use similar numbers of experiments to explore a much narrower parameter space, [34,55] highlighting the value of BO in LPE optimization.

The results of this study also reveal that the optimal inputs for ethanol-based WJM exfoliation of graphene are markedly different than previous reports using other solvent systems. [17,18,22] For example, Del Rio Castillo et al. and several later demonstrations perform WJM exfoliation with a concentration of 1 wt% graphite powder in NMP. In contrast, we find an immense advantage in increasing the graphite loading to 15 wt%. While NMP and watersurfactant systems likely cannot sustain such high loadings during WJM exfoliation, the high loadings permitted by the ethanol-EC system translate into a significantly enhanced graphene production throughput of 3.2 g hr<sup>-1</sup>. Thus, by optimizing the WJM process for graphene exfoliation in ethanol, we can surpass the throughput of incumbent WJM demonstrations. In the following sections, we quantify flake quality, printed device performance, and environmental impact using the optimized WIM processing conditions for graphene nanoplatelet production in ethanol-EC.

NANO · MICRO SMOIL www.small-journal.com

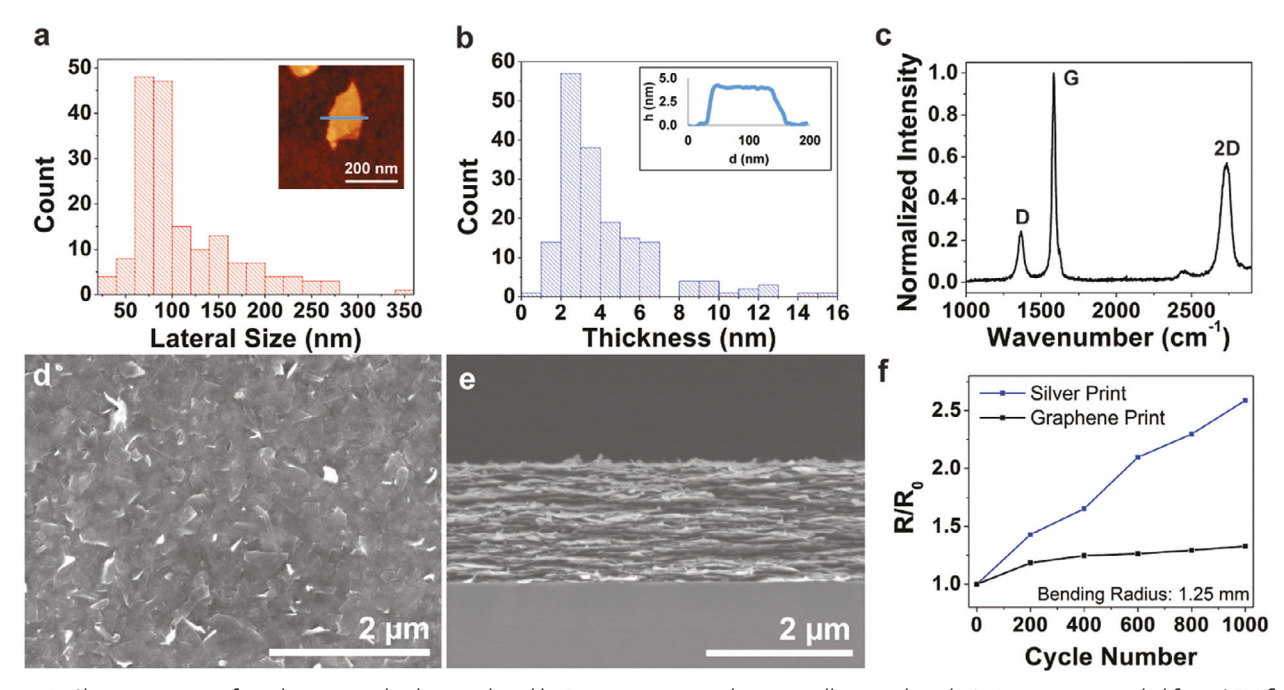


**Figure 4.** Characterization of graphene nanoplatelets produced by Bayesian optimized wet jet milling in ethanol. a) Histogram compiled from AFM flake analysis showing the lateral size distribution (n = 174 flakes). Inset: AFM image of a typical exfoliated graphene flake. b) Histogram compiled from AFM flake analysis showing the flake thickness distribution. Inset: Height profile of the flake shown in the previous inset. c) Raman spectrum of a spin-coated graphene film. SEM micrographs of d) the top surface and e) the cross-section of a graphene film. f) Change in sheet resistance as a function of the bending cycle around a rod with a radius of 1.25 mm for screen-printed graphene and silver films.

#### 3.2. Graphene Flake Characterization

Figure 4 summarizes the properties of the graphene nanoplatelets, which were measured using a suite of characterization techniques. AFM indicates a mean flake thickness of 4.2 nm and a mean flake lateral size of 110 nm (Figure 4a,b), which are consistent with previous reports of graphene nanoplatelets produced via LPE methods in the ethanol-EC system.  $^{[6,56,57]}$  The Raman spectrum shows an  $\rm I_D/I_G$ ratio of 0.27 (Figure 4c), which is also consistent with numerous reports of LPE-produced graphene nanoplatelets, and indicates low defect density as well as a nanosheet population rich in sp<sup>2</sup>carbon.[30,33,54] Scanning electron microscopy (SEM) images of both the top surface and cross-section of the graphene film indicate excellent flake morphology and dense stacking (Figure 4d,e), which are important for achieving efficient charge transport and high electrical conductivity in percolating films. [26] Furthermore, bending tests were performed to evaluate the suitability of the screen-printed features to be employed in flexible electronics. A relatively small 32.8% increase in sheet resistance compared to the unbent film (R/R<sub>0</sub>) was recorded after 1000 bending cycles at a bending radius of 1.25 mm. In contrast, the sheet resistance increased by 159% when a printed silver nanoparticle film was subjected to the same bending conditions (Figure 4f). This factor of five increase in sheet resistance for the silver print compared to the graphene print demonstrates the superior mechanical resilience of the high-aspect-ratio graphene flakes during bending. Overall, these results validate the suitability of WJM-produced ethanol-EC graphene inks for high-performance flexible electronics applications.

#### 3.3. Screen-Printed Micro-Supercapacitors

In this section, we fabricate a device platform that utilizes the superlative electronic properties of the WJM-produced graphene inks. Micro-supercapacitors are high-power energy storage devices with long cycle lifetimes that far exceed rechargeable batteries.<sup>[58,59]</sup> Graphene is a promising material for supercapacitor electrodes due to its high surface area, electrical conductivity, and mechanical strength. [60,61] After WJM exfoliation and purification, the EC-coated graphene nanoplatelets were incorporated into a high-concentration ink for screen printing using terpineol as a solvent. Further characterization of the ink, including thermogravimetric analysis and viscosity measurements, is included in Figures S4 and S5 (Supporting Information). This ink was used for high-throughput patterned deposition of micro-supercapacitor interdigitated electrodes on a polyimide substrate. After the interdigitated electrodes were screen-printed and cured, a PVA-H<sub>3</sub>PO<sub>4</sub> gel electrolyte was carefully drop-casted onto the fingers of the device and dried in the air. A photograph of the completed micro-supercapacitor device and an optical micrograph of the graphene electrodes are provided in Figure 5a. The device performance was then characterized using cyclic voltammetry and galvanostatic charge-discharge measurements. The printed micro-supercapacitors display excellent cycling behavior as shown by the near-rectangular cyclic voltammograms and triangular galvanostatic curves (Figure 5b,c). An areal capacitance of 513  $\mu F\ cm^{-2}$  is achieved at a scan rate of 10 mV  $s^{-1}$ and drops to 315  $\mu F$  cm<sup>-2</sup> at a scan rate of 500 mV s<sup>-1</sup>. This performance is competitive with state-of-the-art graphene micro-supercapacitors and indicates the viability of

and-conditions) on Wiley Online Library for rules of use; OA articles are governed by the applicable Creative Commons



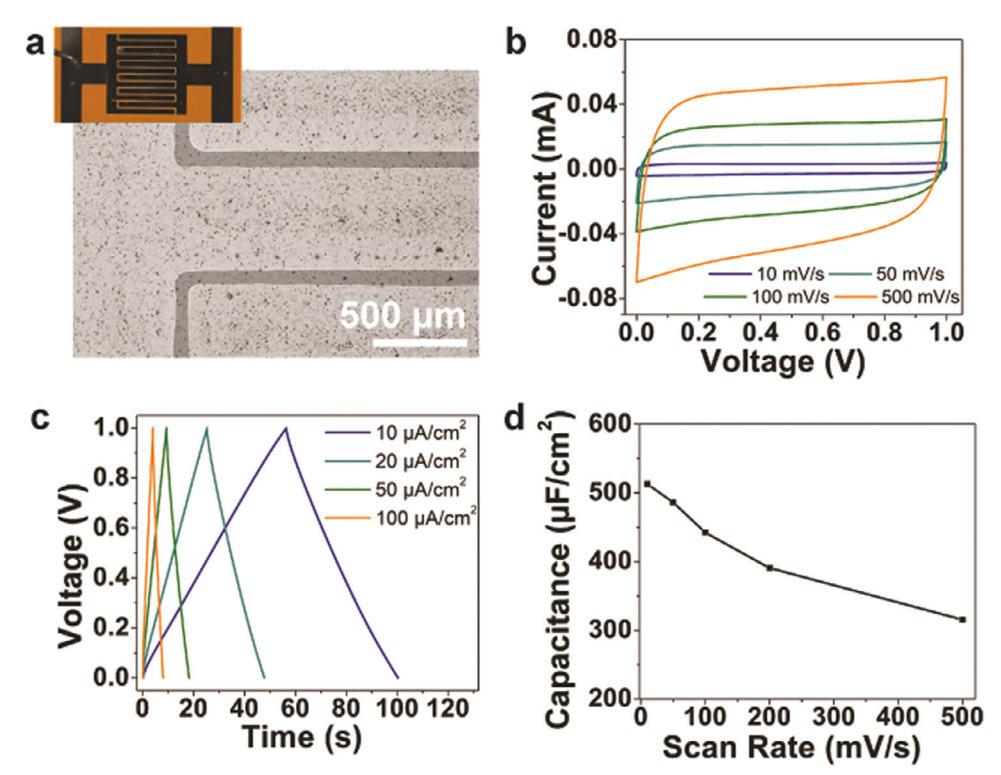


**Figure 5.** Micro-supercapacitors prepared from the optimized graphene ink. a) Photograph and optical micrograph of screen-printed graphene microsupercapacitor electrodes. b) Cyclic voltammograms of the devices at multiple scan rates. c) Galvanostatic charge—discharge curves at multiple current densities. d) The rate capability of the device as quantified by the calculated capacitance at various scan rates.

using WJM-produced graphene inks for high-quality conductive electrodes.

## 4. Life Cycle Assessment

In this section, we quantify the sustainability benefits of scalable graphene production using ethanol-based WIM exfoliation. Figure 6 shows the comparative WJM life cycle assessment (LCA) results for ethanol-based versus NMP-based graphene exfoliation. [65,66] The ethanol-based exfoliation values were calculated based on the optimal yield numbers determined in this study, while the NMP-based exfoliation values were extracted from the leading literature report by Del Rio Castillo et al.[17] (Table S1, Supporting Information). Since both cases use the same exfoliation and centrifugation equipment, the LCA system boundary for comparison purposes is set at the input of the exfoliation process (Figure S6, Supporting Information). The LCA functional unit is the production of inputs to yield one gram of exfoliated graphene in dispersion (Table S2, Supporting Information). Detailed information for life cycle inventory, environmental impacts for each material, and a system boundary diagram can be found in the Supporting Information.

Using cellulosic ethanol rather than NMP as the exfoliation solvent reduces GHG emissions and fossil fuel energy consumption by 95% and 96%, respectively. Two factors contribute to these substantial improvements. First, we achieved  $\approx\!3.5\text{-fold}$  higher yield in this study compared to Del Rio Castillo et al. through our Bayesian optimization of the ethanol-EC exfoliation system. In particular, we found that increasing the graphite

loading drastically improves yield and results in less required solvent per gram of graphene than NMP (Table S1, Supporting Information). Second, NMP is more energy-intensive to produce than ethanol. Specifically, NMP consumes  $\approx$ 25 times more fossil energy and produces  $\approx$ 12 times more greenhouse gases per kilogram compared to ethanol (Table S3, Supporting Information).

Similarly, human toxicity potential, freshwater human toxicity, and freshwater eco-toxicity are each reduced by an order of magnitude when using ethanol instead of NMP. The toxicity potential of both solvents is quantified relative to 1 kg 1,4-Dichlorobenzene (kg 1,4-DCB-eq/kg). The eco-toxicity level (freshwater) and human toxicity level (freshwater) of ethanol and NMP are based on USEtox. [66] The unit for human toxicity level (freshwater) is expressed in comparative toxic units (CTUcancer), which is the estimated increase in morbidity of cancer in the total human population, per unit mass of a chemical emitted to freshwater. The unit for eco-toxicity level (freshwater) is expressed in comparative toxic units (CTUe), which is an estimate of the potentially affected fraction of species (PAF) integrated over time and volume, per unit mass of a chemical emitted to freshwater. The substantial improvement in toxicity risk when replacing NMP with ethanol is due to eliminating the well-known risks associated with NMP. A 2022 report by the U.S. Environmental Protection Agency found NMP to present an unreasonable risk to human health and recommends that risk management regulations be taken imminently.<sup>[67]</sup> Indeed, the European Union has already taken regulatory action by limiting the amount of NMP in consumer products to mitigate toxicity risks.<sup>[68]</sup> These factors make

and-conditions) on Wiley Online Library for rules of use; OA articles are governed by the applicable Creative Commons

www.advancedsciencenews.com

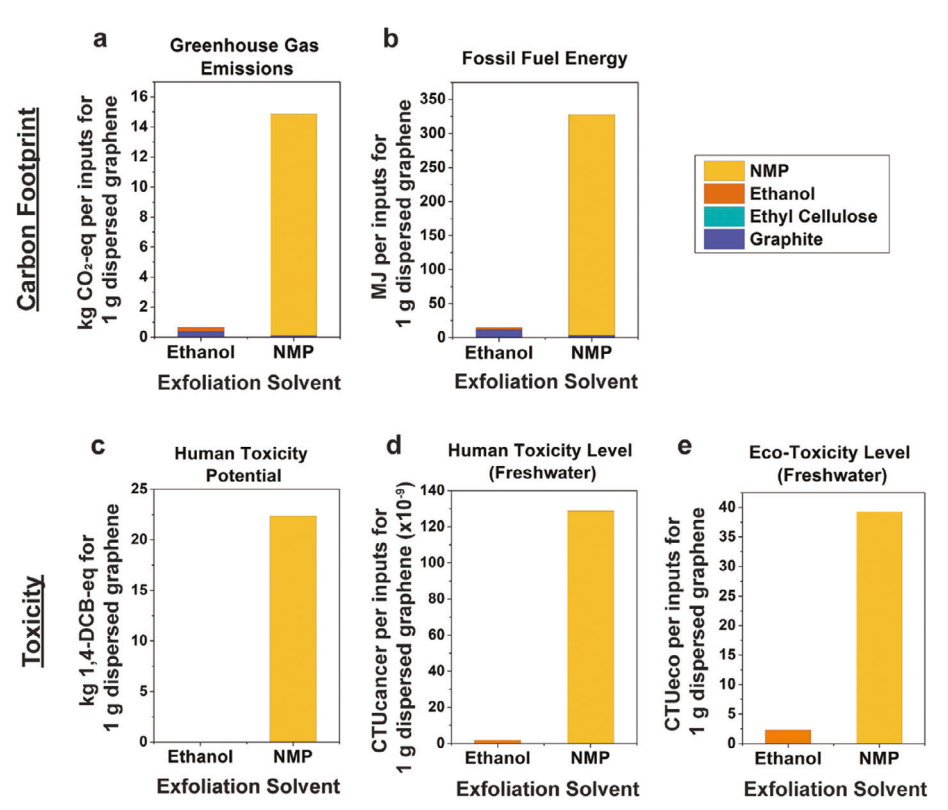


Figure 6. Life cycle assessment. A comparison of the WJM LCA results per 1 gram of exfoliated graphene in dispersion for the ethanol-based exfoliation is presented here versus the incumbent NMP-based exfoliation. The plotted LCA metrics are a) greenhouse gas emissions (GHGs), b) fossil fuel energy, c) human toxicity potential, d) freshwater human toxicity level, and e) freshwater eco-toxicity level.

clear that replacing NMP with ethanol as an exfoliation solvent is critical for the sustainable manufacturing of LPE graphene conductive inks. Figure S7 (Supporting Information) presents additional LCA comparisons.

Additionally, we calculated cradle-to-gate GHG emissions, fossil fuel consumption, and water consumption for producing one gram of exfoliated graphene in dispersion, which includes equipment operation for both exfoliation and purification. The level of electricity consumption for this equipment depends largely on the percent of the time the air compressor and chiller operate, which is between 10% and 50% of the total processing time. We therefore estimate that producing one gram of exfoliated graphite consumes 3.1–15 MJ fossil energy and 1.9–9.5 kg water in addition to emitting 0.22–1.1 kg CO<sub>2</sub>-eq GHGs (Table S4, Supporting Information). Since these energy consumption estimates were obtained from bench-scale operations, it is likely that economies of scale in industrial production will lead to further benefits.

## 5. Conclusion

The rapid growth of the printed electronics industry promises a future with widespread devices and sensors with clear societal benefits. In this study, we improved the sustainability of graphene-based conductive inks by improving wet jet milling for graphene exfoliation in the benign solvent ethanol. In situations where experiment costs are nontrivial, data-driven processing design increases data efficiency, reduces the time required to fully

understand a design space, and ultimately expedites the time to bring products to market. Specifically, by using Bayesian optimization combined with Gaussian process modeling, we identified an unprecedented set of optimized exfoliation conditions, resulting in superlative graphene production rates of 3.2 g hr<sup>-1</sup> while maintaining state-of-the-art electronic properties including a percolating film conductivity of  $4 \times 10^4$  S m<sup>-1</sup>. Moreover, we demonstrated that the resulting graphene conductive inks yield screen-printed micro-supercapacitor devices with highly competitive performance metrics compared to other graphene devices. Finally, using life cycle assessment, we quantified the significant environmental advantages derived from using ethanol in place of NMP during exfoliation, including an order of magnitude lower GHG emissions, fossil fuel energy consumption, and toxicity. Overall, this study demonstrates that a deeper understanding of the connections between multiple experimental inputs and their property responses allows efficient identification of processing parameters to maximize performance, sustainability, and commercial viability.

## 6. Experimental Section

Wet Jet Milling Optimization Testing: Graphene was exfoliated from graphite using a Sugino Star Burst Labo (HJP-25005V2) wet jet mill. For each sample, 750 mL of ethanol (Decon Labs, 200 proof) was mixed with the appropriate ratio of ethyl cellulose (EC, Sigma Aldrich, 4 cP) and graphite (Asbury Carbons, Micro-450). The input loadings for each sample

\_\_\_ SMQII

www.small-journal.com

were dictated by the BO-guided experimental design. The graphite dispersion was then passed through the wet jet mill for a total of ten passes (15 min). To sediment out unexfoliated graphitic material, the sample was centrifuged (Beckman Coulter, Avanti J-26 XPI) at an RCF of  $\approx 10\,000\,g$  for 30 min, as in previous work.  $^{[6]}$  The collected supernatant was then flocculated by adding a 0.04 g mL $^{-1}$  NaCl solution followed by centrifugation at  $\approx 10\,000\,g$  for 7 min. The resulting graphene-EC powder was then rinsed with deionized water and dried for storage and later used in conductive ink formulation.

Graphene Characterization: To determine graphene yield (concentration of the graphene dispersion), optical absorbance spectra were measured using UV/Vis spectroscopy (Agilent, Cary-5000), where concentration was extracted according to Beer's Law. Atomic force microscopy (Asylum Research, Cypher) was used to collect flake images and extract flake population statistics. AFM samples were prepared by drop-casting diluted graphene dispersions onto precleaned Si/SiO2 wafers followed by heating on a hot plate at 350 °C for 30 min. To measure graphene film conductivity, 20 mg mL<sup>-1</sup> of the graphene-EC composite powder was dispersed in a 1:9 mixture of ethyl lactate:ethanol and spin-coated onto 7 mm × 7 mm square glass substrates. The films were thermally cured at 350 °C for 30 min in a box furnace. Sheet resistance was measured using a fourpoint probe measurement system (Lucas Signatone Resistivity Measurement Stand, S-302-4) and a source meter (Keithley, Model 2400). The thickness of the sample was measured using a profilometer (Veeco, Dektak 150). Raman spectroscopy (Horiba, Xplora) was performed on the spin-coated graphene films using a 532 nm laser. Scanning electron microscopy (Hitachi, SU8030) was performed on the top surface of spincoated graphene films. Screen printing was used to form a thicker percolating film of graphene flakes for easier cross-sectional imaging in SEM. A screen-printing ink composed of 120 mg mL<sup>-1</sup> graphene-EC in terpineol (Sigma Aldrich) was formulated and homogenized using a centrifugal mixer (Thinky USA, ARE-310) with ceramic ball bearings for 60 min at increasing speeds from 500 to 2000 rpm. Films were screen-printed (Hary Manufacturing Inc., 886 PC DSIV) onto polyimide substrates and then cured in a box furnace at 350 °C for 30 min.

Bending tests were performed on screen-printed graphene and silver nanoparticle films on polyimide substrates. The graphene was screen-printed as described above. The silver ink (Creative Materials, Inc., 125-13) was screen-printed using the same condition, but the thermal curing occurred at 180  $^{\circ}\text{C}$  for 5 min according to manufacturer guidelines. The printed films were bent around a rod with a radius of 1.25 mm for 1000 bending cycles, and four-point probe measurements were taken in triplicate every 200 cycles.

*Micro-Supercapacitor Fabrication and Characterization*: The graphene interdigitated micro-supercapacitor electrodes were screen-printed with the following dimensions: 500 μm wide fingers, 5.5 mm long fingers, 150 μm gaps, 12 total fingers, and overall dimensions of 7.65 mm × 7.65 mm. Afterward, a PVA-containing gel electrolyte was prepared by mixing 0.75 g of PVA (MW 89000-98000, Sigma Aldrich) with 0.5 g of phosphoric acid (85%, Sigma Aldrich) and 4.5 mL of deionized water. The resulting PVA-H $_3$ PO $_4$  gel electrolyte was carefully drop-casted onto the fingers of the device followed by drying in air. Electrochemical characterization tests, including cyclic voltammetry and galvanostatic chargedischarge tests, were performed using a potentiostat (BioLogic, VSP).

# **Supporting Information**

Supporting Information is available from the Wiley Online Library or from the author.

# Acknowledgements

L.E.C. acknowledges Keisuke Yoneda and Motohide Ho from Sugino Corp. for their expertise and assistance in the operation of the WJM. This work was primarily supported by the National Science Foundation MADE-PUBLIC Future Manufacturing Research Grant Program

(NSF Award Number CMMI-2037026). Additional support for the microsupercapacitor fabrication and testing was provided by the U.S. Department of Commerce, National Institute of Standards and Technology (Award No. 70NANB19H005) as part of the Center for Hierarchical Materials Design (CHiMaD). This work made use of the EPIC Facility within the Northwestern University NUANCE Center, which has received support from the SHyNE Resource (NSF ECCS-2025633), the International Institute for Nanotechnology, and the Northwestern University MRSEC (NSF DMR-2308691).

#### **Conflict of Interest**

The authors declare no conflict of interest.

## **Data Availability Statement**

The data that support the findings of this study are available from the corresponding author upon reasonable request.

## **Keywords**

conductive inks, life cycle assessment, liquid phase exfoliation, printed electronics, screen printing

Received: October 22, 2023 Revised: February 24, 2024 Published online: March 26, 2024

- S. Agarwala, G. L. Goh, T. S. Dinh Le, J. An, Z. K. Peh, W. Y. Yeong, Y. J. Kim, ACS Sens. 2019, 4, 218.
- [2] D. Liu, J. Wang, L. Wu, Y. Huang, Y. Zhang, M. Zhu, Y. Wang, Z. Zhu, C. Yang, TrAC – Trends Anal. Chem. 2020, 122, 115701.
- [3] X. Sui, J. R. Downing, M. C. Hersam, J. Chen, *Mater. Today* **2021**, *48*,
- [4] A. Kamyshny, S. Magdassi, Small 2014, 10, 3515.
- [5] E. B. Secor, M. C. Hersam, J. Phys. Chem. Lett. 2015, 6, 620.
- [6] E. B. Secor, P. L. Prabhumirashi, K. Puntambekar, M. L. Geier, M. C. Hersam, J. Phys. Chem. Lett. 2013, 4, 1347.
- [7] E. Jabari, E. Toyserkani, Mater. Lett. 2016, 174, 40.
- [8] T. Seifert, E. Sowade, F. Roscher, M. Wiemer, T. Gessner, R. R. Baumann, Ind. Eng. Chem. Res. 2015, 54, 769.
- [9] P. He, J. Cao, H. Ding, C. Liu, J. Neilson, Z. Li, I. A. Kinloch, B. Derby, ACS Appl. Mater. Interfaces 2019, 11, 32225.
- [10] C. Lee, X. Wei, J. W. Kysar, J. Hone, Science 2008, 321, 385.
- [11] W. Yang, C. Wang, J. Mater. Chem. C 2016, 4, 7193.
- [12] N. O. Weiss, H. Zhou, L. Liao, Y. Liu, S. Jiang, Y. Huang, X. Duan, Adv. Mater. 2012, 24, 5782.
- [13] K. S. Novoselov, V. I. Fal'ko, L. Colombo, P. R. Gellert, M. G. Schwab, K. Kim, *Nature* **2012**, *490*, 192.
- [14] L. Niu, J. N. Coleman, H. Zhang, H. Shin, M. Chhowalla, Z. Zheng, Small 2016, 12, 272.
- [15] F. Withers, H. Yang, L. Britnell, A. P. Rooney, E. Lewis, A. Felten, C. R. Woods, V. Sanchez Romaguera, T. Georgiou, A. Eckmann, Y. J. Kim, S. G. Yeates, S. J. Haigh, A. K. Geim, K. S. Novoselov, C. Casiraghi, *Nano Lett.* 2014, 14, 3987.
- [16] J. R. Downing, S. Diaz-Arauzo, L. E. Chaney, D. Tsai, J. Hui, J. T. Seo, D. R. Cohen, M. Dango, J. Zhang, N. X. Williams, J. H. Qian, J. B. Dunn, M. C. Hersam, *Adv. Mater.* 2023, *35*, 2212042.
- [17] A. E. Del Rio Castillo, V. Pellegrini, A. Ansaldo, F. Ricciardella, H. Sun, L. Marasco, J. Buha, Z. Dang, L. Gagliani, E. Lago, N. Curreli,



www.small-journal.com

- S. Gentiluomo, F. Palazon, M. Prato, R. Oropesa-Nuñez, P. S. Toth, E. Mantero, M. Crugliano, A. Gamucci, A. Tomadin, M. Polini, F. Bonaccorso, *Mater. Horizons* **2018**, *5*, 890.
- [18] S. Bellani, E. Petroni, A. E. Del Rio Castillo, N. Curreli, B. Martín-García, R. Oropesa-Nuñez, M. Prato, F. Bonaccorso, Adv. Funct. Mater. 2019, 29, 1807659.
- [19] T. Onodera, C. Kannari, A. Koyano, Y. Furukawa, K. Mitake, F. Yasuda, F. Miyake, Jokoh Co Ltd., US5,984,519A 1999.
- [20] N. Omura, Y. Hotta, K. Sato, Y. Kinemuchi, S. Kume, K. Watari, J. Am. Ceram. Soc. 2006, 89, 2738.
- [21] Y. Tominaga, K. Sato, D. Shimamoto, Y. Imai, Y. Hotta, Ceram. Int. 2015, 41, 10512.
- [22] R. Malik, Q. Huang, L. Silvestri, D. Liu, V. Pellegrini, L. Marasco, E. Venezia, S. Abouali, F. Bonaccorso, M. J. Lain, D. Greenwood, G. West, P. R. Shearing, M. J. Loveridge, 2D Mater. 2021, 8, 015012.
- [23] Y. Hernandez, V. Nicolosi, M. Lotya, F. M. Blighe, Z. Sun, S. De, I. T. McGovern, B. Holland, M. Byrne, Y. K. Gun'Ko, J. J. Boland, P. Niraj, G. Duesberg, S. Krishnamurthy, R. Goodhue, J. Hutchison, V. Scardaci, A. C. Ferrari, J. N. Coleman, *Nat. Nanotechnol.* 2008, 3, 563.
- [24] J. Shen, Y. He, J. Wu, C. Gao, K. Keyshar, X. Zhang, Y. Yang, M. Ye, R. Vajtai, J. Lou, P. M. Ajayan, *Nano Lett.* 2015, 15, 5449.
- [25] J. Coleman, Science 2011, 331, 568.
- [26] S. Barwich, J. Medeiros de Araújo, A. Rafferty, C. Gomes da Rocha, M. S. Ferreira, J. N. Coleman, Carbon 2021, 171, 306.
- [27] X. Han, J. Gao, T. Chen, Y. Zhao, Chem. Pap. 2020, 74, 757.
- [28] N. D. Mansukhani, L. M. Guiney, P. J. Kim, Y. Zhao, D. Alducin, A. Ponce, E. Larios, M. J. Yacaman, M. C. Hersam, Small 2016, 12, 294
- [29] Y. T. Liang, M. C. Hersam, J. Am. Chem. Soc. 2010, 132, 17661.
- [30] A. C. M. de Moraes, J. Obrzut, V. K. Sangwan, J. R. Downing, L. E. Chaney, D. K. Patel, R. E. Elmquist, M. C. Hersam, J. Mater. Chem. C 2020, 8, 15086.
- [31] E. B. Secor, B. Y. Ahn, T. Z. Gao, J. A. Lewis, M. C. Hersam, Adv. Mater. 2015, 27, 6683.
- [32] M. L. Green, I. Takeuchi, J. R. Hattrick-Simpers, J. Appl. Phys. 2013, 113, 231101
- [33] K. R. Paton, E. Varrla, C. Backes, R. J. Smith, U. Khan, A. O'Neill, C. Boland, M. Lotya, O. M. Istrate, P. King, T. Higgins, S. Barwich, P. May, P. Puczkarski, I. Ahmed, M. Moebius, H. Pettersson, E. Long, J. Coelho, S. E. O'Brien, E. K. McGuire, B. M. Sanchez, G. S. Duesberg, N. McEvoy, T. J. Pennycook, C. Downing, A. Crossley, V. Nicolosi, J. N. Coleman, *Nat. Mater.* 2014, *13*, 624.
- [34] U. Khan, A. O'Neill, M. Lotya, S. De, J. N. Coleman, Small 2010, 6, 864.
- [35] M. J. Large, S. P. Ogilvie, A. Amorim Graf, P. J. Lynch, M. A. O'Mara, T. Waters, I. Jurewicz, J. P. Salvage, A. B. Dalton, Adv. Mater. Technol. 2020, 5, 2000284.
- [36] R. Leardi, Anal. Chim. Acta 2009, 652, 161.
- [37] E. Stach, B. DeCost, A. G. Kusne, J. Hattrick-Simpers, K. A. Brown, K. G. Reyes, J. Schrier, S. Billinge, T. Buonassisi, I. Foster, C. P. Gomes, J. M. Gregoire, A. Mehta, J. Montoya, E. Olivetti, C. Park, E. Rotenberg, S. K. Saikin, S. Smullin, V. Stanev, B. Maruyama, *Matter* 2021, 4, 2702.
- [38] L. Liu, Z. Shen, X. Zhang, H. Ma, J. Colloid Interface Sci. 2021, 582, 12.
- [39] L. Pronzato, W. G. Müller, Stat. Comput. 2012, 22, 681.
- [40] R. Jin, W. Chen, A. Sudjianto, J. Stat. Plan. Inference 2005, 134, 268.

- [41] В. Математики, USSR Comput. Math. Math. Phys. 1967, 7, 784.
- [42] B. Shang, D. W. Apley, J. Qual. Technol. 2021, 53, 173.
- [43] C. E. Rasmussen, C. K. I. Williams, Gaussian Processes for Machine Learning, University of Edinburgh, UK 2006.
- [44] S. Tao, A. Van Beek, D. W. Apley, W. Chen, J. Mech. Des. Trans. ASME 2021, 143, 111701.
- [45] A. van Beek, U. F. Ghumman, J. Munshi, S. Tao, T. Y. Chien, G. Balasubramanian, M. Plumlee, D. Apley, W. Chen, J. Mech. Des. Trans. ASME 2021, 143, 031709.
- [46] P. Zhu, S. Zhang, W. Chen, Eng. Optim. 2015, 47, 287.
- [47] M. C. Kennedy, A. O'Hagan, J. R. Stat. Soc. Ser. B Stat. Methodol. 2001, 63, 425.
- [48] A. van Beek, S. Tao, M. Plumlee, D. W. Apley, W. Chen, J. Mech. Des. 2020, 142, 031114.
- [49] D. R. Jones, J. Glob. Optim. 2001, 21, 345.
- [50] P. I. Frazier, W. B. Powell, S. Dayanik, 2008, 47, 2410.
- [51] J. M. Hernández-Lobato, M. W. Hoffman, Z. Ghahramani, Adv. Neural Inform. Process. Syst. 2014, 27, 918.
- [52] D. Huang, T. T. Allen, W. I. Notz, N. Zeng, J. Glob. Optim. 2006, 34, 441.
- [53] F. Bonaccorso, A. Lombardo, T. Hasan, Z. Sun, L. Colombo, A. C. Ferrari, Mater. Today 2012, 15, 564.
- [54] T. Carey, A. Alhourani, R. Tian, S. Seyedin, A. Arbab, J. Maughan, L. Šiller, D. Horvath, A. Kelly, H. Kaur, E. Caffrey, J. M. Kim, H. R. Hagland, J. N. Coleman, NPJ 2D Mater. Appl. 2022, 6, 3.
- [55] Y. Arao, M. Kubouchi, Carbon 2015, 95, 802.
- [56] K. Y. Park, J. M. Lim, N. S. Luu, J. R. Downing, S. G. Wallace, L. E. Chaney, H. Yoo, W. J. Hyun, H. U. Kim, M. C. Hersam, Adv. Energy Mater. 2020, 10, 2001216.
- [57] W. J. Hyun, E. B. Secor, M. C. Hersam, C. D. Frisbie, L. F. Francis, Adv. Mater. 2015, 27, 109.
- [58] J. Wang, F. Li, F. Zhu, O. G. Schmidt, Small Methods 2019, 3, 1800367.
- [59] N. Liu, Y. Gao, Small 2017, 13, 1701989.
- [60] C. Wang, M. Muni, V. Strauss, A. Borenstein, X. Chang, A. Huang, S. Qu, K. Sung, T. Gilham, R. B. Kaner, Small 2021, 17, 2006875.
- [61] L. E. Chaney, W. J. Hyun, M. Khalaj, J. Hui, M. C. Hersam, Adv. Mater. 2023, https://doi.org/10.1002/adma.202305161.
- [62] W. J. Hyun, E. B. Secor, C.-H. Kim, M. C. Hersam, L. F. Francis, C. D. Frisbie, Adv. Energy Mater. 2017, 7, 1700285.
- [63] Z. Liu, Z.-S. Wu, S. Yang, R. Dong, X. Feng, K. Müllen, Adv. Mater. 2016, 28, 2217.
- [64] A. P. S. Gaur, W. Xiang, A. Nepal, J. P. Wright, P. Chen, T. Nagaraja, S. Sigdel, B. LaCroix, C. M. Sorensen, S. R. Das, ACS Appl. Energy Mater. 2021, 4, 7632.
- [65] International Organization for Standardization, ISO 14040:2006 Environmental Management — Life Cycle Assessment — Principles and Framework, https://www.iso.org/standard/37456.html, (accessed: December 2021).
- [66] United States Environmental Protection Agency. Tool for Reduction and Assessment of Chemicals and Other Environmental Impacts (TRACI) 2022, https://www.epa.gov/chemical-research/toolreduction-and-assessment-chemicals-and-other-environmentalimpacts-traci (accessed: February 2023).
- [67] C. Chen, V. Reddy, H. Lin, L. Shaw, J. Energy Chem. 2023, 78, 240.
- [68] J. Sherwood, T. J. Farmer, J. H. Clark, Chem 2018, 4, 2010.